Analysis and Modelling of Power-Dependent Harmonic Characteristics of Modern PE Devices in LV Networks

Analysis and Modelling of Power-Dependent Harmonic Characteristics of Modern PE Devices in LV Networks

Xu Xiao, Adam J. Collin, *Member, IEEE*, Sasa Z. Djokic, *Senior Member, IEEE*,
Sergey Yanchenko, Friedemann Möller, Jan Meyer, *Member, IEEE*,
Roberto Langella, *Senior Member, IEEE*, and Alfredo Testa, *Fellow, IEEE*

***Abstract*—This paper presents results of experimental and analytical evaluation of power-dependent harmonic emission of three common types of modern low voltage (LV) power electronic (PE) devices. After a detailed analysis of comprehensive test results, based on both existing and new waveform distortion indices, the development of component-based models of PE devices is discussed. The paper demonstrates the importance of including PE devices' controls for accurate modelling of their characteristics over the entire range of operating powers. Most of the analysed PE devices exhibit strong power-dependent changes of characteristics, additionally influenced by supply voltage conditions, which are important for the analysis of both existing networks and future "smart grids".**

***Index Terms*—Harmonic analysis, modelling, power quality, power electronics, smart grid, testing, waveform distortion.**

I. Introduction

An increasing number of modern low voltage (LV) power electronic (PE) devices utilize high-frequency switching circuits and complex controls for improved performance, better reactive power regulation and increased efficiency. Common examples of power-consuming PE devices are switch-mode power supplies (SMPS') and electric vehicle battery chargers (EVBCs) with active power factor control (a-PFC) circuits. In the case of power-generating LV PE devices, the most common technology is photovoltaic inverters (PVIs) with pulse-width modulated (PWM) control.

The harmonic emissions of PE equipment are governed by well-established international standards, e.g. [1-3] in the EU, [4] in the US and [5] in Australia and New Zealand. Most of the relevant standards, however, specify that harmonic emission tests of LV PE devices shall be conducted under sinusoidal voltage supply conditions with equipment operating at the rated power, P_{rated}, or at maximum total harmonic current in amps [1]. Identical test conditions are specified for EVBCs, with [6-7] citing [1-2] for harmonic compliance testing of EVBCs, despite the fact that the power during the charging cycle is variable, and will typically reduce during the latter stages. Test procedures for power-generating LV PE devices do consider variable power operation, with [3] and [5] specifying test points at 100% and 50% (and 25% in [3]) of P_{rated} for PVIs. However, the actual output of any PVI can be, and often is lower, dependent on ambient conditions.

Across the operating range, the performance of the internal control circuits of a PE device may be compromised, altering the device's characteristics. This may have a negative impact on the supply grid when such equipment is connected in large numbers. This paper presents a detailed experimental-based characterization of a number of SMPS', EVBCs and PVIs across their entire operational ranges and for different supply conditions. Two new indices are introduced for the analysis, which allow separate assessment of the contributions from the low-frequency (LF) harmonics and all other waveform distortions to the device's total operating current. This is of particular importance for the analysis of modern PE devices, for which LF harmonics might not be the most significant part of the total waveform distortion (e.g. [8]). The analysis of measurements is supported by the development of component-based (circuit-based) models, capable of correctly reproducing the harmonic characteristics over the entire operating range.

This paper shows that mostof tested PE devices exhibit distinctive power-dependent performance changes. The impact of realistic supply voltage conditions, i.e. distorted voltage and source impedance, on device characteristics is also considered and is shown to have considerable impact on certain types of equipment. Particular attention is given to the increased distortion in low and very low power operating modes (defined as below 30% and 10% of P_{rated}), as this issue has received limited attention in literature and is not fully captured by existing indices. When operating in very low power mode, some of the measured PE devices enter unstable operating regions or disconnect (i.e. 'trip' via their internal protection). These effects signify the importance of PE devices' controls when evaluating and modelling power-dependent changes in their performance. All model parameter values are listed in the appendix, to allow reproduction of the presented results.

The experimental and analytical frameworks are presented in Section II and illustrated on measured data in Section III. Section IV describes the model development process. Section V provides conclusions and areas of further work.

The authors gratefully acknowledge support by German Federal Ministry BMUB (FKZ: 16EM1052, ElmoNetQ) and Italian Campania Region project POLIGRID.

X. Xiao, A. J. Collin and S. Z. Djokic are with the University of Edinburgh, Edinburgh, Scotland, U.K. (e-mail: sasa.djokic@ed.ac.uk).

S. Yanchenko is with the Moscow Power Engineering Institute, Moscow, Russia (e-mail: yanchenkosa@mpei.ru)

F. Möller and J. Meyer are with the Technische Universitaet Dresden, Dresden, Germany (e-mail: jan.meyer@tu-dresden.de).

R. Langella and A. Testa are with the Dept. of Ind. and Inf. Eng, The 2nd University of Naples, Aversa, Italy (e-mail: roberto.langella@unina2.it).

II. Experimental and Analytical Frameworks

A. Current Waveform Distortion Indices Used for Analysis

1) *Existing harmonic distortion indices:* Current harmonic distortion of PE devices can be presented in absolute values, denoted as total harmonic current *THC*, (1), or in relative values, either as total harmonic distortion of current THD_I, (2), or as the total demand distortion *TDD*, (3). As *THC* and *TDD* are related by a constant factor ($100/I_{rated}$) and have similar meaning, only *THC* and THD_I are considered for further analysis in this paper.

$$THC = \sqrt{\sum_{h=2}^{H} (I_h)^2} \tag{1}$$

$$THD_I = \frac{1}{I_{fund}} \sqrt{\sum_{h=2}^{H} (I_h)^2} \times 100 = \frac{THC}{I_{fund}} \times 100 \tag{2}$$

$$TDD = \frac{1}{I_{rated}} \sqrt{\sum_{h=2}^{H} (I_h)^2} \times 100 = \frac{THC}{I_{rated}} \times 100 \tag{3}$$

where: I_{rated}, I_{fund}, and I_h are the r.m.s. values of the rated current, the fundamental component and the current harmonic of order *h*, respectively. The maximum considered harmonic order *H* is typically 40 or 50, representing LF harmonics.

THC and *THD* indices allow to perform harmonic emission analysis from two different perspectives. *THC* allows analysis of the impact of emissions on voltage harmonic levels in the network (i.e. network perspective) for studying, e.g. electromagnetic compatibility or evaluating the contribution of PE devices to the total harmonic distortion. THD_I assesses the harmonic performance of an individual PE device (i.e. equipment perspective), indicating how the device's harmonic currents change in relation to the fundamental current, which is important for equipment manufacturers and end-users.

In this paper, the power-dependent changes in harmonic emissions are assessed by calculating $I_{fund}(P)$ and $I_h(P)$, and then $THC(P)$ and $THD_I(P)$ at a given operating power *P*.

2) *Existing waveform distortion indices:* Expressions (1)-(3) typically assess only harmonic emissions and do not take into account other types of waveform distortion, which might be present in modern PE devices, e.g. sub-harmonics, inter-harmonics and higher frequency emissions [9]. For evaluating the total current waveform distortion, [10] defines the fundamental factor, FF, and the total distortion content, TDC (4)-(5). In this paper, these are also considered as functions of the device operating power.

The $FF(P)$ and $TDC(P)$ indices evaluate the power-dependency of the contributions of fundamental and non-fundamental currents to the total operating current of the PE device. The *TDC* index includes all distortions, regardless of the considered frequency range, with reference to the total operating current. As it is possible to extract the fundamental component without DFT/FFT analysis, e.g. [11], *FF* and *TDC* do not suffer from spectral leakage problems [12]. Moreover, *TDC* quantifies how effectively modern LV PE devices control their total current waveform distortion. This is important as a design objective, and therefore a way to compare the performance of different PE devices, and as an operational requirement, due to stipulated limits in, e.g. [1-5].

$$FF(P) = \frac{I_{fund}(P)}{I_{tot}(P)} \tag{4}$$

$$TDC(P) = \frac{I_{non\_fund}(P)}{I_{tot}(P)} = \frac{\sqrt{I_{tot}^2(P) - I_{fund}^2(P)}}{I_{tot}(P)} = \sqrt{1 - FF^2(P)} \tag{5}$$

where: $I_{tot}(P)$, $I_{fund}(P)$ and $I_{non\_fund}(P)$ are the r.m.s values of: the total current, fundamental current and non-fundamental current, respectively, at given operating power *P*.

3) Two new waveform distortion indices: To allow for a more detailed analysis, this paper introduces two new indices: the total harmonic factor, restricted to LF harmonics, THF_{LF} (6), and the total non-(LF)-harmonic distortion factor, *TNHDF* (7). These indices accompany the previously introduced *TDC* and *FF* indices and extend their application.

The value of two new indices lies is in their ability to make a further distinction between the contributions of the LF harmonics and all other distortions. As shown later in the paper, this is of particular importance for the analysis of modern PE devices, for which LF harmonics might not be the most significant part of the total waveform distortion.

$$THF_{LF}(P) = \frac{THC(P)}{I_{tot}(P)} = \frac{THD_I(P) \cdot FF(P)}{100} \tag{6}$$

$$TNHDF(P) = \frac{I_{non\_harm}(P)}{I_{tot}(P)} = \frac{\sqrt{I_{tot}^2(P) - I_{fund}^2(P) - THC^2(P)}}{I_{tot}(P)} = \sqrt{1 - FF^2(P) \cdot (1 + (THD_I(P)/100)^2)} \tag{7}$$

where $I_{non\text{-}harm}(P)$ is the rms values of non-LF-harmonic (non-fundamental) distortion current at given operating power *P*.

B. Test Set-Up and Test Parameters

A fully automated test-bed, with accuracies better than 5%, 2% and 1% for individual harmonic magnitudes higher than 50mA, 100mA and 200mA, respectively, is used for all tests [8]. It consisted of a 1MS/s acquisition system and a controllable three-phase power source with programmable voltage waveforms and source impedance values, allowing configuration of specific waveform-impedance combinations. The testing is controlled from a centralized workstation with respect to two test parameters:

1) *The source impedance value:* was set to either a) the minimum possible source impedance, ZS1≈0 (due to the impedance of a cable connecting the PE device to the power source and the power source itself) or b) the maximum expected LV network source impedance ZS2, consisting of Z_{phase}= (0.24 + j0.15) Ω and $Z_{neutral}$= (0.16 + j0.10) Ω [13].

2) The ac supply voltage waveform: was emulated as an ideally sinusoidal reference waveform (WF1) and as two distorted voltage waveforms (WF2 and WF3). The two distorted waveforms are derived from the measurements in LV networks and have different harmonic magnitudes and phase angles (further information is available in [14]). The "flat-top" WF2 is typical of a network supplying a large number of residential customers with 2-pulse rectifiers, while the "pointed-top" WF3 is typical for LV networks with a large number of industrial customers with 6-pulse rectifiers [15].

The two distorted waveforms used for testing include phase angle variations, which are known to influence the operation of PE control circuits. Further information on the impact of phase angle dependencies and cross-coupling of harmonics on the emission of PVIs and EVBCs can be found e.g. in [16-18].

III. Measurement Results

A. PV Inverters (PVIs)

The three measured PVIs include both single-phase and three-phase types, featuring transformerless, LF and HF transformer topologies. Figs. 1a and 1b show that the *THC* values for two out of the three PVIs do not reduce at lower power outputs, while the corresponding *THD* values suggest that their harmonic emissions might be of concern. For example, *THC*(*P*) values of PVI-1 for WF1 and ZS1 start to increase in low power mode, resulting in *THC* values higher than at 75% of P_{rated} and almost equal to values at P_{rated}. All three PVIs have very low *THD* values at high operating powers for WF1 and ZS1. In very low power mode, however, their *THD*(*P*) values increase up to 100 times. These changes would not be identified if the tests were performed with the operating powers set at 50% [3] or 25% [5] of P_{rated}.

The presence of supply voltage distortion and source impedance might have a very strong impact. *THC(P)* values of PVI-2 for WF2-3 and ZS2 increase several times with respect to the *THC(P)* values for WF1 and ZS1 (note a six-fold *THC* increase in Fig. 1b and logarithmic scale in Fig. 1a). Similarly, *THC(P)* values of PVI-1 for WF2-3 and ZS2 are 50% higher than *THC(P)* for WF1 and ZS1, with *THC* at 20% of P_{rated} almost equal to *THC* at 75% of P_{rated}. Moreover, in very low power mode, *THD(P)* values of PVI-2 for WF2 and ZS2 are almost 600% and the device will disconnect from the supply, indicating that PVI-2 cannot control its harmonic emission in very low power mode when connected to grids with typical background distortion and source impedance values.

The $THF_{LF}(P)$ and *TNHDF(P)* indices introduced in this paper provide further insights into the sources of the harmonic distortion. The contribution of the fundamental current of all tested PVIs to their total operating current starts to decrease around 25% of P_{rated} (most notably for PVI-2, Fig. 1c). In very low power mode, the non-fundamental currents of all PVIs are several times higher than their fundamental currents. For example, Fig. 1d shows that a significant part of current waveform distortion of PVI-3 is not due to LF harmonics. These results clearly indicate that if only LF-harmonic-related indices (*THD*, *THC* and/or *TDD*) are used for the analysis, this might not result in a full assessment of the current waveform distortions of modern PE devices.

B. Switch-Mode Power Supplies (SMPS')

Test results for two SMPS' with a-PFC circuits (standard desktop PC supplies) at different powers are shown in Fig. 2. In very low power operating mode, SMPS-2 enters unstable operating conditions, which prevented further testing. To analyze the whole range of operating powers, a component-based SMPS model is developed in the next section and used to complement the available test results. Fig. 2a shows noticeable changes in the harmonic performance of the two tested SMPS' in low power mode. The results for SMPS-1 show that its harmonic currents in the very low power mode are almost equal to its fundamental currents (*THD* of 80-100%), although the *THC* values of both SMPS' in Fig. 2b exhibit continuous reduction with decreasing operating power.

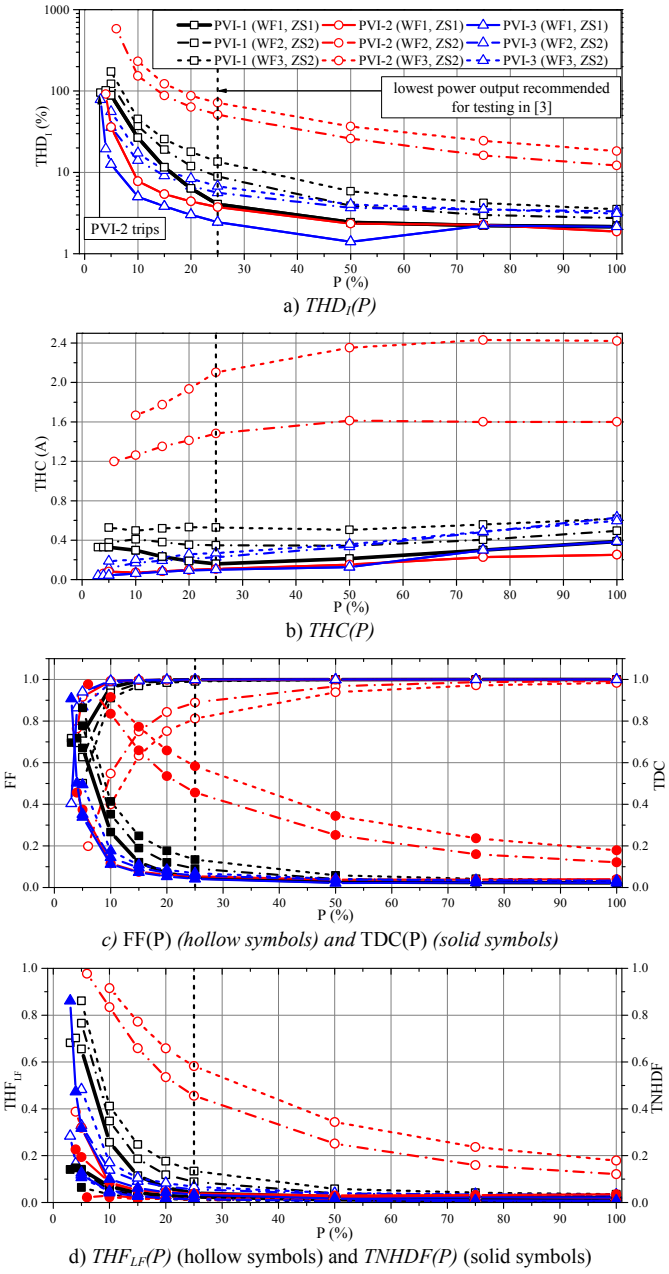

a) $THD_I(P)$

b) *THC(P)*

c) FF(P) *(hollow symbols) and* TDC(P) *(solid symbols)*

d) $THF_{LF}(P)$ (hollow symbols) and *TNHDF(P)* (solid symbols)

Fig. 1. Power-dependent waveform distortion indices of the tested PVIs.

The impact of supply voltage distortions is less pronounced than for PVIs, with SMPS-2 displaying negligible change. For SMPS-1, with reference to WF1 (sinusoidal), THD_I decreases for the "flat-top" WF2 and increases for the "pointed-top" WF3, while *THC* reduces for both WF2 and WF3. Fig. 2c shows that the contribution of the fundamental current to the total current of SMPS-1 starts to decrease in low power mode, becoming equal to the contribution of the non-fundamental current in very low power mode, as indicated by the *THD*(*P*) values in Fig. 2a. Fig. 2d presents the contributions from the LF harmonics and other current waveform distortion to the total current, confirming that LF harmonics (THF_{LF}) have the largest contribution to the waveform distortion, as non-LF-harmonic distortion (*TNHDF*) remains very small for all considered WFs and ZS values.

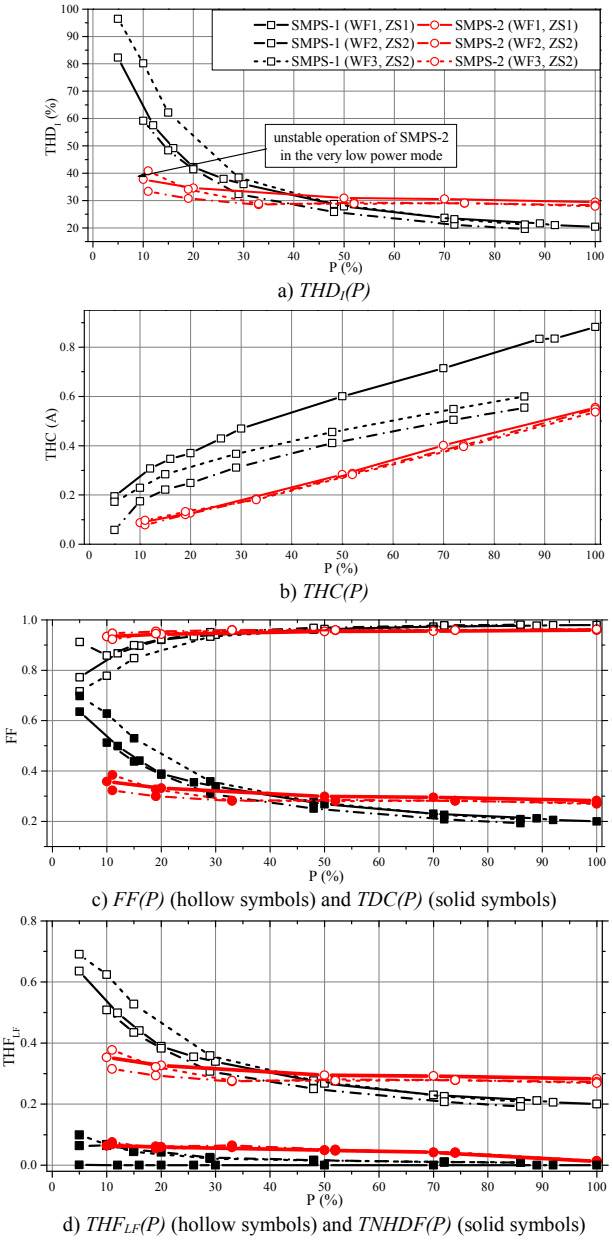

Fig. 2. Power-dependent waveform distortion indices of the tested SMPS'.

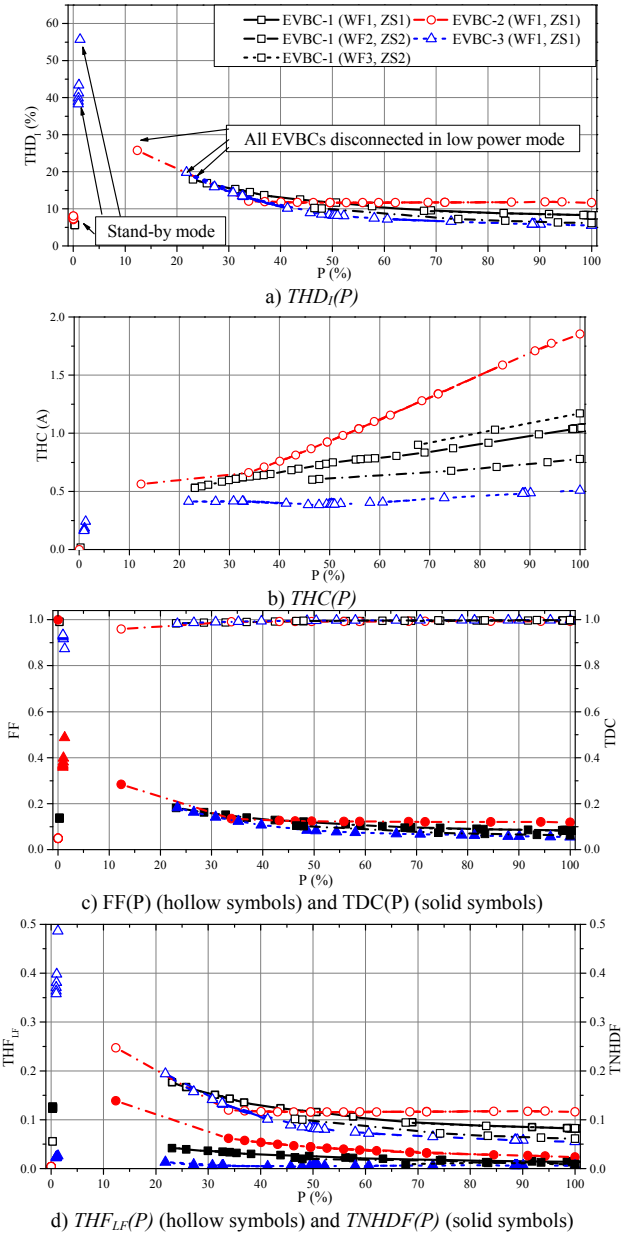

Fig. 3. Power-dependent waveform distortion indices of the tested EVBCs.

C. EV Battery Chargers (EVBCs)

The three EVs, which are available in the EU market, were subject to tests in which their on-board single-phase Level-2 chargers were measured during the standard charging cycle. Based on the state-of-charge of the EV battery, the EVBCs first operated at rated power (constant-current, CC, mode) and then transferred to constant-voltage (CV) mode, characterized by the reduced power demands. In CV mode, the control disconnected the EVBCs at low operating powers (indicated in Fig. 3a), preventing analysis for the entire operating range (see the EVBC model developed in Section IV for further results).

Fig. 3a shows that the *THD* values of all EVBCs start to increase in low power mode. Some high *THD* values are measured in "stand-by" mode, i.e. when charging is finished but the EVBC is still connected to the supply. However, this is not considered further due to the negligible power demands. Similar to the SMPS', there is very little effect of supply voltage distortion and source impedance.

The *THC* plots in Fig. 3b indicate that the absolute harmonic currents of two EVBCs steadily decrease with reduced powers. For EVBC-3, however, after an initial reduction there is a slight increase of *THC* below 40% of P_{rated}. Fig. 3c shows that the contribution of the fundamental current of the tested EVBCs is somewhat reduced in (very) low power mode, with limited contribution of non-fundamental currents. In other words, the measured EVBCs have much better control of current waveform distortion than the PVIs and SMPS'. The available THF_{LF} in Fig. 3d confirm that LF harmonics are the main contributor to the total waveform distortion, as the *TNHDF* values are very low.

IV. Modelling of Modern PE Devices

Building on the previous work of the authors (e.g. [14-15]), this section presents the development of component-based SMPS, EVBC and PVI models, capable of accurately reproducing their current waveform distortion characteristics over the entire range of operating powers and for different supply conditions. The models are derived in a general form, in order to represent generic PE devices that are currently available on the EU domestic market, but model parameters have been adjusted to match the tested PE devices and to validate simulation results with the measurement results. All model parameters are included in the appendix.

A. Modelling of SMPS'

Fig. 4 shows the developed component-based SMPS model, consisting of an input EMI filter, standard diode bridge rectifier (DBR) and dc-dc boost converter with a-PFC circuit. The modelled EMI filter is a balanced "T filter", which, together with the a-PFC circuit, controls EMI and harmonic emission in accordance with prescribed limits e.g. [1]. After the DBR, there is a small input capacitor for stabilizing the input voltage in accordance with the peak current requirement of the SMPS [19]. The boost converter and the a-PFC circuit determine the power-dependent changes in the current waveform distortion characteristics of the modelled SMPS, since they directly regulate both the output dc voltage and input inductor current (and, therefore, the input ac current).

Fig. 5 details the a-PFC circuit developed as an important part of the SMPS model. It uses average current mode control, consisting of an inner current loop and an outer voltage loop. For the outer voltage loop, the sensed output voltage, is scaled down and then compared with its reference value. The difference, i.e. the voltage error, is supplied to the voltage controller, whose output is multiplied with the haversine function, which is scaled down from the input voltage to produce the inductor current reference waveform. The scaled inductor current is compared with its reference waveform, with the difference fed to the current controller. Finally, the output of the current controller is compared with a high-frequency sawtooth signal to generate the PWM control signal for the boost converter switch. Additional information on the developed SMPS model and its parameters are given in [15] and in Table A.I in the appendix.

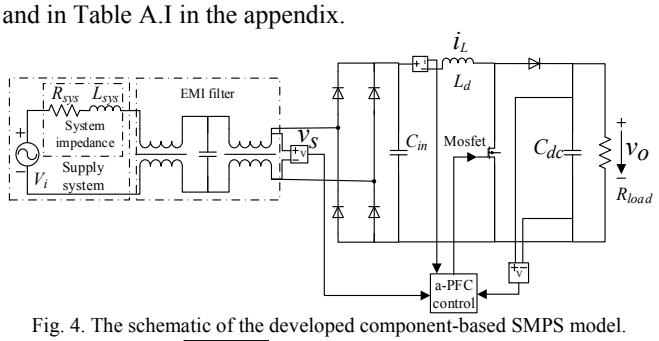

Fig. 4. The schematic of the developed component-based SMPS model.

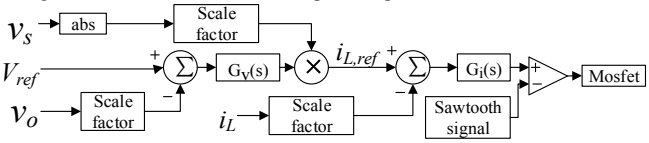

Fig. 5. The block diagram of a-PFC circuit applied to the SMPS model.

B. SMPS Model Validation and Discussion

To validate the developed SMPS model, the model parameters were set to emulate the characteristics of SMPS-2 from Section III.B. Good matching between the measured and simulated input ac current waveforms for different operating powers and supply conditions in Fig. 6 suggests that the developed model is capable of correctly reproducing the current waveform distortion characteristics of the real device.

Transfer of the a-PFC control from continuous conduction mode (CCM) to discontinuous conduction mode (DCM) is the main reason for increased waveform distortion of the input ac current at low and very low operating powers, Figs. 6a-6c. During the DCM operation, the inductor current is often zero during the switching cycle, as the a-PFC controller is unable to follow its reference waveform. If the a-PFC circuit is not properly integrated with the SMPS model, it would be very difficult to obtain good matching between the simulation and measurements results. Fig. 6d provides an example (only for illustrative purposes), comparing the results for the developed SMPS model with and without the a-PFC circuit (in the EU market, SMPS with P_{rated}<75W may not include a-PFC [1]).

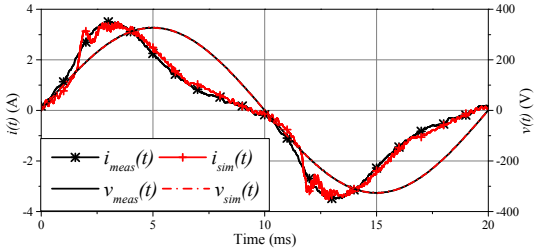

a) input ac voltage WF1 and ZS1, *v(t)*, and current, *i(t)*, at 100% P_{rated}

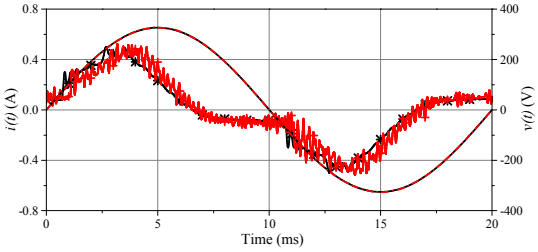

b) input ac voltage WF1 and ZS1, *v(t)*, and current, *i(t)*, at 10% P_{rated}

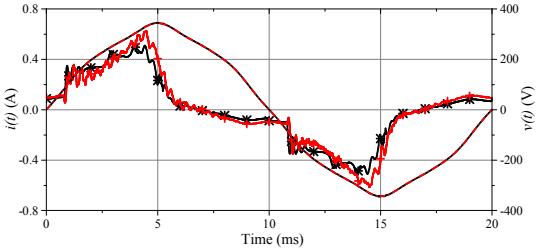

c) input ac voltage WF3 and ZS2, *v(t)*, and current, *i(t)*, at 10% P_{rated}

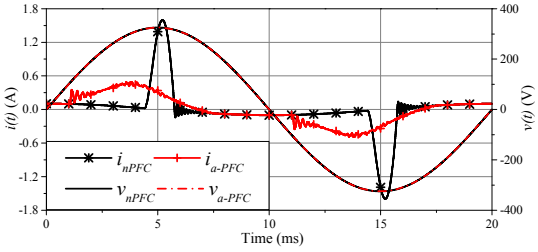

d) input ac voltage WF1 and ZS1, *v(t)*, and current, *i(t)*, at 10% P_{rated} with and without a-PFC circuit

Fig. 6. Comparison of measurement ("meas") and simulation ("sim") results in time domain for SMPS-2 at two different power levels.

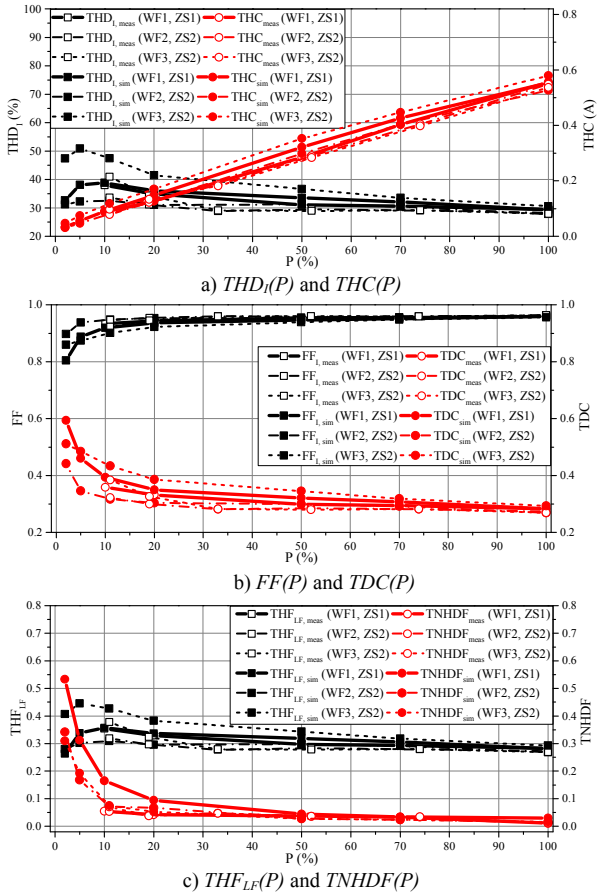

a) $THD_I(P)$ and $THC(P)$

b) $FF(P)$ and $TDC(P)$

c) $THF_{LF}(P)$ and $TNHDF(P)$

Fig. 7. Comparison of measured ("meas", hollow symbols) and simulated ("sim", solid symbols) waveform distortion indices of SMPS-2.

Fig. 7 compares measurement and simulation results for all previously discussed current waveform distortion indices, again demonstrating a very good match. Furthermore, the simulation results with the SMPS model complement the test results (not available in very low power mode due to the unstable operation of SMPS-2) and suggest, for example, a stronger contribution of non-LF-harmonics to the total waveform distortion below around 10% of P_{rated} in Fig. 7c.

C. Modelling of EVBCs

Fig. 8 shows the developed component-based EVBC model. Its front-end circuit is similar to the previously presented SMPS model, as it also consists of an EMI filter, DBR, dc-dc boost converter and dedicated control circuits. The main differences are in the EMI filter and the a-PFC circuit. The EMI filter in the EVBC model uses an L filter (i.e. an RC low-pass filter), while the EVBC a-PFC circuit utilizes a modified peak current mode control, shown in Fig. 9.

The a-PFC circuit allocates an upper and lower boundary for the control of the inductor current, which should be maintained between these two limits. When the inductor current is above the lower boundary, the a-PFC control turns into a normal peak current control. Additionally, the applied modified peak current control neglects the voltage control loop and sets the reference magnitude of the input current directly in the current control loop. More details on the developed EVBC model can be found in [14], with parameter values included in Table A.I in the appendix.

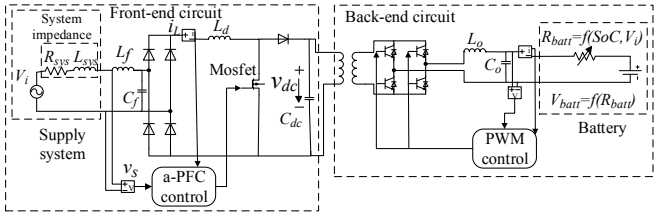

Fig. 8. The schematic of the developed component-based EVBC model.

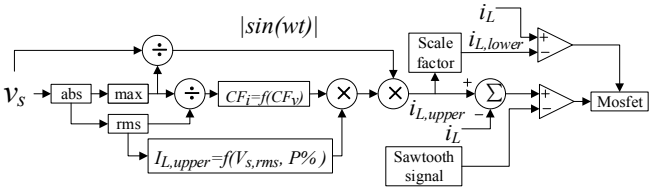

Fig. 9. The block diagram of a-PFC control applied to the EVBC model.

D. EVBC Model Validation and Discussion

The developed EVBC model (with parameters adjusted to EVBC-1 from Section III.C) is again validated by comparing measured and simulated input ac current waveforms, Fig. 10. Again, good matching between the results in the time-domain is obtained for all supply and operating conditions.

Although there is a higher distortion and ripple content in the instantaneous ac current in low power mode, its waveform is much better regulated by the modelled EVBC's a-PFC circuit, than in the case of SMPS (see also Section IV.G). It can be concluded that the a-PFC (i.e. type, circuit topology, control strategy and control settings) will determine harmonic emission and waveform distortion characteristics. In the case of the EVBC, the a-PFC basically controls input ac current waveform to emulate the input ac voltage waveform.

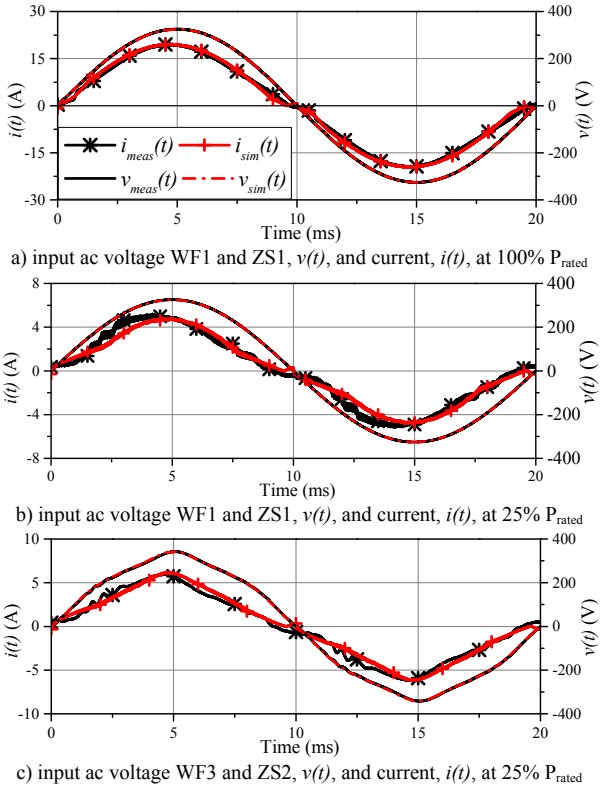

a) input ac voltage WF1 and ZS1, $v(t)$, and current, $i(t)$, at 100% P_{rated}

b) input ac voltage WF1 and ZS1, $v(t)$, and current, $i(t)$, at 25% P_{rated}

c) input ac voltage WF3 and ZS2, $v(t)$, and current, $i(t)$, at 25% P_{rated}

Fig. 10. Comparison of measurement ("meas") and simulation ("sim") results in time domain for EVBC-1 at two different power levels.

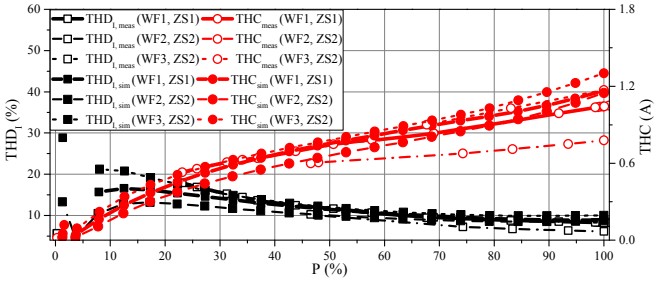

a) *THD$_I$(P)* and *THC(P)*

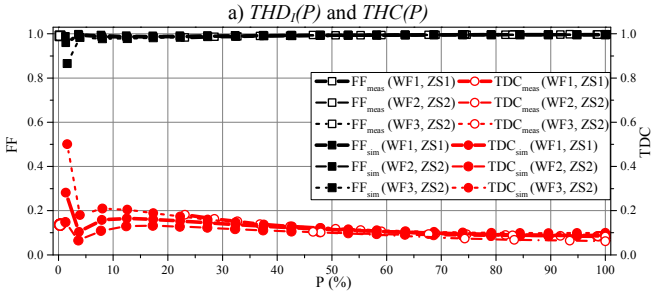

b) FF(P) *and* TDC(P)

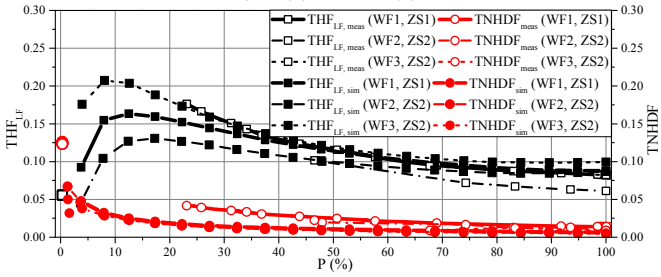

c) *THF$_{LF}$(P)* and *TNHDF(P)*

Fig. 11. Comparison of measured ("meas", hollow symbols) and simulated ("sim", solid symbols) waveform distortion indices of EVBC-1.

Fig. 11 compares measurement and simulation results for waveform distortion indices, again showing good agreement between the two sets of data. Generally, the results of the simulation complement the available test results in very low power mode, as Fig. 3 shows that CV charging can stop at powers as low as 10% of P_{rated}. More importantly, Fig. 11 shows the complex behaviour of the modelled PE device in the very low power mode, which is discussed in Section IV.G.

E. Modelling of PVIs

The developed component-based PVI model is illustrated in Fig. 12. It consists of a PV panel (represented by a controlled current source), dc-side capacitor, full bridge inverter and its control circuit and output filter. The control of the full bridge innverter is shown in Fig. 13 and can be divided into two parts. The grid synchronization part detects the instantaneous ac supply voltage waveform and applies an *abc* to *dq* transform as input into a PLL for determining the synchronous reference frame into the closed loop control. The grid current control consists of an inner current loop (in *αβ* stationary reference frame, SRF, and a PR controller) and an outer voltage loop (with the reference for the grid current magnitude realised by a PI controller). At the output, a scale factor multiplies the averaged three-phase reference voltage waveforms at the full bridge inverter terminals, which are fed to the inverter model. More details of the SRF-PLL control model can be found in [20] and in Table A.I in the appendix.

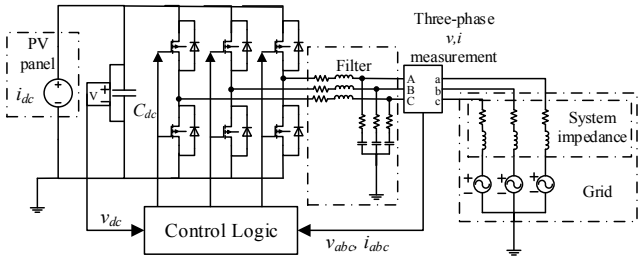

Fig. 12. The schematic of the developed component-based PVI model.

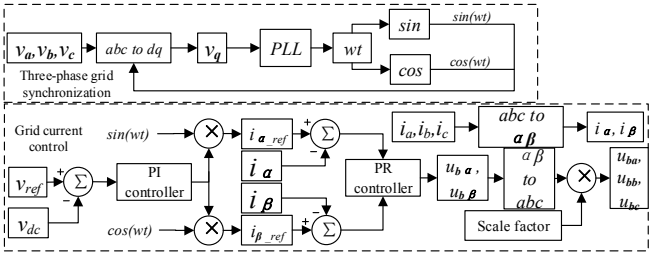

Fig. 13. The block diagram of PVI model control.

F. PVI Model Validation and Discussion

The developed PVI model (with parameters adjusted to PVI-2 from Section III.A) is again validated by comparing measured and simulated ac current waveforms, Fig. 14. As for the two previously considered types of modern PE devices, the presented results indicate that the developed component-based PVI model is capable of correctly representing the power-dependent harmonic and waveform distortion characteristics for different operating and supply conditions.

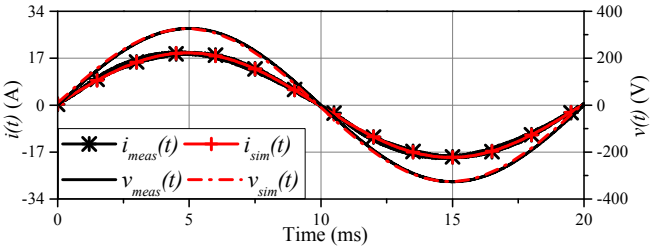

a) instantaneous ac voltage WF1 and ZS1, *v(t)*, and current, *i(t)*, at 100% P_{rated}

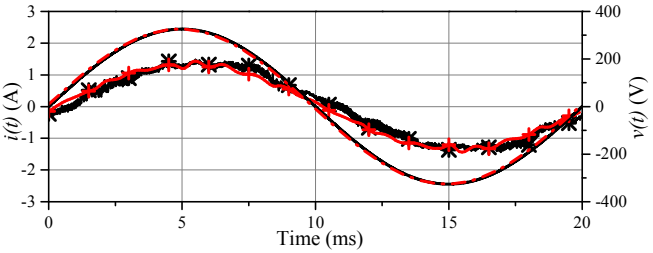

b) instantaneous ac voltage WF1 and ZS1, *v(t)*, and current, *i(t)*, at 10% P_{rated}

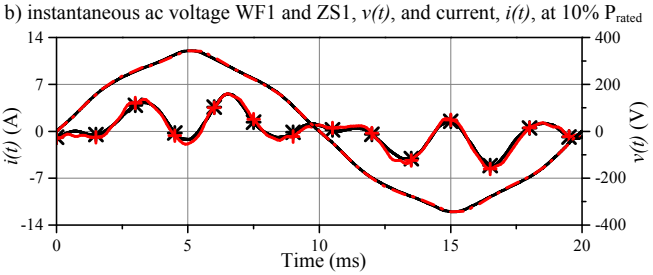

c) instantaneous ac voltage WF3 and ZS2, *v(t)*, and current, *i(t)*, at 10% P_{rated}

Fig. 14. Comparison of measurement ("meas") and simulation ("sim") results in time domain for PVI-2 at two different power levels.

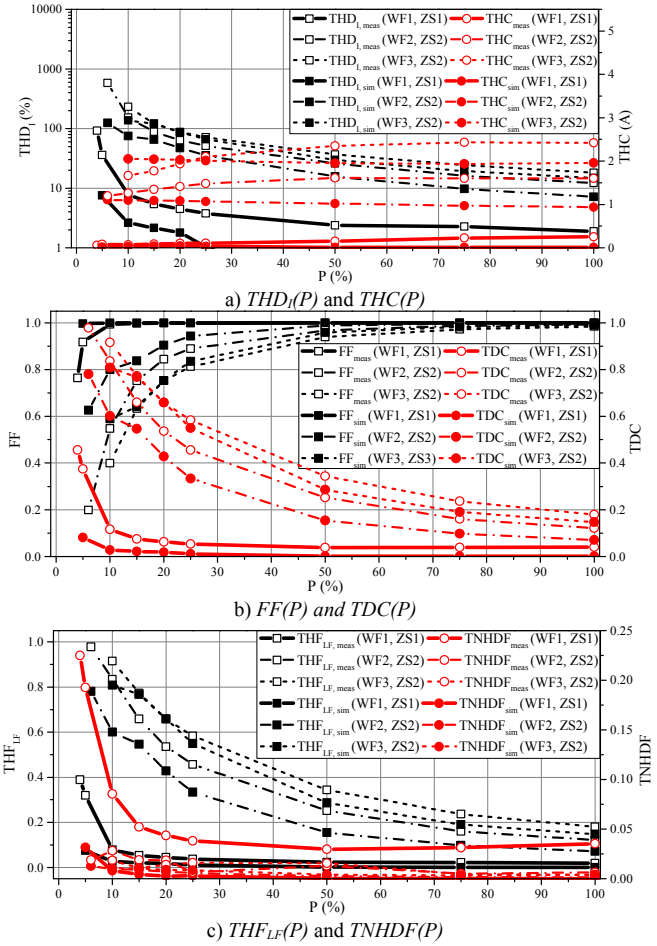

Fig. 15. Comparison of measured ("meas", hollow symbols) and simulated ("sim", solid symbols) waveform distortion indices of PVI-2.

Comparing the results in Figs. 14a and 14b shows an increase of distortion and a more pronounced ripple in the instantaneous ac current in very low power mode, while Fig. 14c demonstrates the inability of the PVI's a-PFC circuit to control its output ac current in the presence of supply voltage distortion. The main reason for that is a relatively low gain of the PR current controller (adjusted to match the measured results for PVI-2), resulting in unstable operation due to the deviation of the controller output from the reference value in case of the distorted supply voltage. The shape of the PVI output current results from a trade-off in the control system, which is balancing the accuracy of the produced current control signal with the ability to maintain stable operation under the input filter resonances [21]. The unstable operation of PVI-2 is captured by the developed model, with Fig. 15 showing again a good matching of measurements and simulations for all considered waveform distortion indices.

G. On the Importance of Modelling Controls of PE Devices

Fig. 16 provides more details on the transfer of SMPS-2 from CCM to DCM operation (Section IV.B). As the SMPS power reduces, the modelled a-PFC control strategy (average current control) cannot maintain the inductor current above the zero value, even after increasing the frequency of switching. On the other hand, the modelled peak current control of the a-PFC circuit of EVBC-1 successfully maintains the inductor current between the upper and lower boundary, Fig. 17.

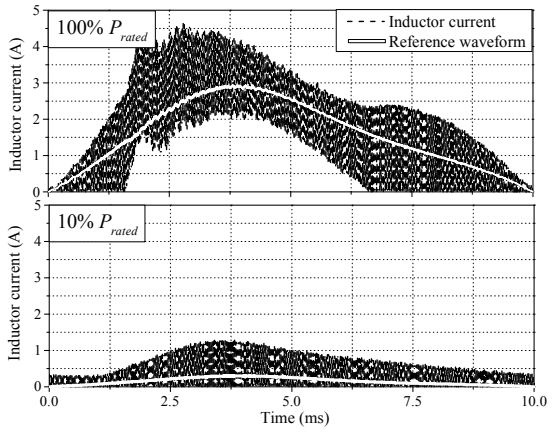

Fig. 16. SMPS inductor current and its reference waveform for WF1 and ZS1.

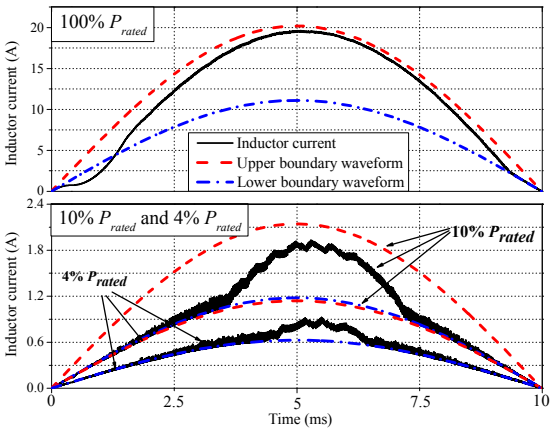

Fig. 17. EVBC inductor current and its reference waveform for WF1 and ZS1.

Fig. 17 also illustrates the complex behaviour of EVBC-1 as its operating power reduces from 100% to 10% of P_{rated}, and then to 4% of P_{rated}. Waveform distortion will first increase, due to pulse-like part in the middle of the half-cycle current waveform, but will then decrease, due to the alignment of the inductor current with the lower boundary.

Although both EVBC and SMPS contain a-PFC controlled front-end circuits, the EVBC has a more effective control. As a result, the harmonic characteristics presented to the network are considerably different, demonstrating the importance of the correct modelling of the a-PFC control for the evaluation of waveform distortion characteristics of modern PE devices.

V. Conclusions and Further Work

Increasing numbers and installed powers of modern PE devices require careful assessment of their impact on both existing networks and future "smart grids". Modern PE devices implement sophisticated controls, marking significant difference from the period as recent as one decade ago, when most PE equipment had only simple circuit topologies, without any PFC, or with only passive PFC circuit implemented in equipment design.

The results presented in this paper are limited in terms of the types and numbers of considered PE devices, as well as analyzed supply and operating conditions. Although further work is needed to identify and quantify possibly much wider range(s) of responses, the following conclusions can be drawn from the presented experimental and analytical evaluation.

Most of the analyzed PE devices exhibit distinctive increase of relative harmonic emission in low power operating modes, which may become very high at very low powers. Two PVIs and one EVBC also increased their absolute harmonic emission at low powers. This suggests that the impact of individual PE devices could increase if they simultaneously enter low power operating modes, e.g. due to daily variations of PVI outputs, or "smart grid" coordinated EVBC control. One example of a nuisance tripping of protection systems due to PVIs operation in low power mode is given in [22].

For most (but not all) of the considered operating and supply conditions, the contribution of the fundamental current to the total current of a PE device will start to decrease at low powers, becoming equal to, or lower than the contribution of the non-fundamental current at very low powers. The two new indices introduced in this paper allow separate assessment of the contributions from the LF harmonics and other waveform distortions, highlighting that, in some cases, LF harmonics are not main contributor to the total waveform distortion.

The presence of source impedance and supply voltage waveform distortion, which is typically the case in actual LV grids, might have a strong negative impact on performance of some PE devices (most evident for one of the tested PVIs, which exhibits a six-fold increase of the *THC* values). This suggests that testing of modern PE devices should include non-sinusoidal waveforms, in order to check whether they can control harmonic emission in practical applications.

From the presented analysis, the main reason for increased waveform distortion of modern PE devices with a-PFC in low power operating modes is the transfer from CCM to DCM operation. This might be further pronounced if supply voltage distortions and source impedances are present, as some types of a-PFC will emulate the distorted input ac voltage waveform for setting internal current or voltage references. This clearly suggests that models of PE devices have to integrate control (a-PFC) circuits for correctly representing their characteristics.

Several lines of further work can be specified from the presented analysis. Regarding the experimental part, further tests with both individual and group-connected PE devices are required. Regarding the analytical part, evaluation of smart grid functionalities and wider area network studies will require the development of simplified general ("generic") component-based models, to represent large numbers of same types of PE devices and their controls. When the modelled PE equipment features complex circuits and sophisticated controls (e.g. PVIs or EVBCs), frequency domain modelling allows for a simpler and efficient representation of a large number of modelled devices (e.g. harmonic domain and harmonic state-space approaches). Work is in progress on both aspects (e.g. [23]).

APPENDIX A

TABLE A.I PARAMETERS OF SMPS, EVBC AND PVI MODELS

SMPS-2									
Power stage			**Volt. control loop**			**Volt. scale factor**	**Current control loop**		
C_{in}, µF	L, µH	C_{DC}, µF	Scale factor	V_{ref}, V	$G_V(s)$		Scale factor	$G_I(s)$	K_{PWM}
1.1	780	460	1/400	2.5	$24/(1.8\cdot10^{-3}s+1)$	1/325	0.4	$6.5\cdot10^{3}(2\cdot10^{-5}s+1)/(10^{-6}s^{2}+s)$	0.25

EVBC-1							
Input filter		**Boost converter**		**Filter**		**CC-CV Charging Control**	
L_f, mH	C_f, nF	L_d, mH	C_{dc}, µF	L_o, mH	C_o, µF	I_{ref}, A	V_{ref}, V
0.1	1	11	1300	10	100	6.66	360

PVI-2										
Input Filter				**DC-Link**		**DC-Link Volt. PI Controller**		**Current PR Controller**		
L, mH	R_L, Ω	C, µF	R_C, Ω	C_{DC}, uF	V_{DC}, V	K_P	K_I, s^{-1}	K_P	K_I, s^{-1}	ω_C, s^{-1}
0.85	0.35	12	0.5	600	690	1.1	1	4	90	20

REFERENCES

[1] IEC, *EMC–Part 3-2: Limits for harmonic current emissions (equipment current ≤ 16 A per phase)*, IEC Standard 61000-3-2, 2014.

[2] IEC, *EMC – Part 3-12: Limits for harmonic currents produced by equipment connected to public low-voltage systems with input current > 16 A and ≤ 75 A per phase*, IEC Standard 61000-3-12, 2011.

[3] IEC TR, *EMC – Part 3-15: Limits–Assessment of low frequency electromagnetic immunity and emission requirements for dispersed generation systems in LV networks*, IEC Tech. Report 61000-3-15, 2011.

[4] IEEE, *Recommended Practice and Requirements for Harmonic Control in Electric Power Systems*, IEEE Standard 519, 2014.

[5] AS/NZS, *Grid connection of energy systems via inverters: Part 2: Inverter requirements*, Australian/New Zealand Standard 4777.2, 2015.

[6] IEC, *EV conductive charging system. Part 21: EV requirements for conductive connection to an ac/dc supply*, IEC Std. 61851-21, 2002.

[7] IEC, *LV electrical installations–Part 7-722: Requirements:-Supply of electric vehicle*, Draft IEC Standard 60364-7-722 Ed 1.0, 2014.

[8] R. Langella, A. Testa, J. Meyer, F. Möller, R. Stiegler and S. Z. Djokic, "Experimental based evaluation of PV inverters harmonic and interharmonic distortion due to different operating conditions," *IEEE Trans. Instrumentation and Measurement*, 2016. (in print)

[9] IEC, *Electromagnetic compatibility (EMC). Part 4-7: General guide on harmonics and interharmonics measurements for power supply systems and equipment connected thereto*, IEC Std. 61000-4-7. Ed. 2. 2009.

[10] IEC, *Glossary of Electrotechnical, power, telecommunication, electronics, lighting and colour terms — Part 1: Terms common to power, telecommunications and electronics — Group 09: Electromagnetic compatibility*, IEC Standard 60050-161, 2nd Ed. 1991.

[11] L. Czarnecki, "Two algorithms of the fundamental harmonic complex RMS value calculation," Archiv fur Elektrotechnik 75, 1992.

[12] D.Gallo, R.Langella, and A.Testa, "On the processing of harmonics and interharmonics: using Hanning window in standard framework", *IEEE Trans. on Power Delivery*. Vol. 19, No. 1, Jan. 2004.

[13] IEC, *Consideration of Reference Impedances and Public Supply of Network Impedance for Use in Determining Disturbance Characteristics of Electrical Equipment Having a Rated Current Less Than 75A Per Phase*, IEC Standard 60725, 2005.

[14] X. Xu, M. He, P. Kourtza, A. Collin, G. Harrison S. Z. Djokic, J. Meyer, S. Müller and F. Möller, "Component-based modelling of EV battery chargers" , *IEEE Conf. PowerTech* 2015.

[15] S. Yanchenko and J. Meyer, "Harmonic emission of household devices in presence of typical voltage distortions", *IEEE Conf. PowerTech* 2015.

[16] S. Müller, J. Meyer and P. Schegner: "Characterization of small photovoltaic inverters for harmonic modeling", *ICHQP*, June 2014.

[17] S. Müller, J. Meyer, P. Schegner and S. Djokic: Harmonic modeling of electric vehicle chargers in frequency domain, *ICREPQ*, 2015.

[18] B.C. Smith, N.R. Watson, A.R. Wood and J. Arillaga,'Harmonic tensor linearisation of HVDC Converters", *IEEE Trans. Power Delivery*, vol. 13, no. 4, Oct. '98.

[19] B. Hauke, *Basic Calculation of a Boost Converter's Power Stage*, Texas Instruments Application Report, pp. 1–9, 2014.

[20] R. Teodorescu, M. Liserre and P. Rodriguez, *Grid Converters for Photovoltaic and Wind Power Systems*", John Wiley IEEE, 2011.

[21] B. Terzic, G. Majic, and A. Slutej, "Stability analysis of three-phase PWM converter with LCL filter by means of nonlinear model", *Automatika*, vol. 51, no.3, 2010.

[22] D. Gallo, R. Langella, A. Testa, J. C. Hernández, I. Papič, B. Blažič and J. Meyer, "Case studies on large PV plants: Harmonic distortion, unbalance and their effects", *IEEE PES GM*, 2013, Vancouver, BC.

[23] J. Meyer, S. Müller, P. Schegner, S. Djokic, A. Collin and X. Xu: "Comparison of methods for modelling electric vehicle chargers for harmonic studies", *PSCC*, June 2016. (accepted)